J. Fluid Mech. (1994), *vol.* 261, *pp.* 305–332

Interaction of a turbulent round jet with the free surface

By C. K. MADNIA† AND L. P. BERNAL
Department of Aerospace Engineering, University of Michigan, Ann Arbor, MI 48109-2118, USA

(Received 27 January 1992 and in revised form 8 September 1993)

The interaction of a turbulent round jet with the free surface was investigated experimentally. Flow visualization, free-surface curvature measurements and hot-film velocity measurements were used to study this flow. It is shown that surface waves are generated by the large-scale vortical structures in the jet flow as they interact with the free surface. These waves propagate at an angle with respect to the flow direction which increases as the Froude number is increased. Propagation of the waves in the flow direction is suppressed by the surface current produced by the jet. Farther downstream the surface motions are caused by the large-scale vortical structures. Characteristic dark circular features are observed in shadowgraph images associated with concentrated vorticity normal to the free surface. The normal vorticity is believed to be the result of vortex line reconnection processes in the turbulent flow. Measurements of the mean velocity and turbulence intensity are reported. Owing to the confinement by the free surface, the decay rate of the maximum mean velocity is reduced by a factor of $\sqrt{2}$ compared to an unconfined jet.

1. Introduction

The results of an experimental investigation of the interaction of a submerged turbulent jet with the free surface are presented. The flow geometry and parameters are shown in figure 1. One motivation for this study is to obtain a better understanding of the nature of the free-surface waves and motions caused by the interaction of turbulent shear flows with the surface. These flow processes are an important part of the free-surface signature of the turbulent wake behind a ship. Aerial and space photographs of the sea surface show distinct features which persist for very large distances behind the ship in the viscous wake region (Munk, Scully-Power & Zachariasen 1987). The interaction of a turbulent jet with the free surface is one of the simplest flow configurations which incorporates many of the vortical interactions encountered in the turbulent ship wake problem.

An early experimental investigation of the interaction of a submerged jet with the free surface was conducted by Evans (1955). He demonstrated the calming effect on surface waves caused by the surface currents produced by the jet. Evans study did not consider the details of the turbulent flow structure. He showed that when the waves and currents move in the same direction the wave amplitude is decreased. A theoretical analysis of this phenomenon by Taylor (1955) provides an explanation of these results and further shows that in this case the wavelength of the surface waves is increased. The effect of non-uniform steady surface currents was investigated by Longuet-Higgins

† Present address: Department of Mechanical and Aerospace Engineering, State University of New York at Buffalo, Buffalo, NY 14260, USA.

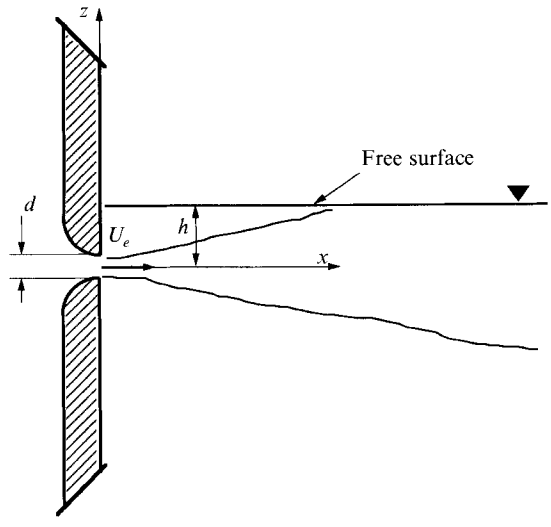

FIGURE 1. Schematic diagram of the flow geometry.

& Stewart (1961) (see also Phillips 1966). They consider different types of non-uniform surface currents and show that if the current is in the same direction as the direction of propagation of the waves the amplitude of the waves decreases. On the other hand if the waves propagate into a region with an opposing surface current the amplitude of the waves increases.

Rajaratnam & Humphries (1984) studied the mean flow characteristics of free-surface jets when the free surface is located at the edge of the jet nozzle, i.e. $h/d = 0.5$. In their investigation they did not study the free-surface motion caused by the jet/free-surface interaction. However, they reported a reduction of the mean velocity near the surface at high Froude numbers which was attributed to surface wave generation. For circular surface jets they confirmed the same scaling for the maximum mean velocity decay as for the free jet or wall jet measurements of Rajaratnam & Pani (1974). Self-similarity was found for the mean velocity profiles. The growth rate in the direction perpendicular to the free surface was found equal to the wall-jet growth rate while the growth rate in the direction parallel to the free surface was found to be approximately half of the wall-jet growth rate. Rajaratnam & Humphries (1984) and more recently Ramberg, Swean & Plesnia (1989) have studied two-dimensional free-surface jets. They also pointed out the similarity with a wall jet in this case. Ramberg *et al.* discussed the effects of jet confinement in their tank. Novikov (1988) discussed the mean surface deformation of the free surface caused by an underwater jet. He did not consider the effect of the velocity fluctuations.

Anthony & Willmarth (1992) measured the mean and fluctuating velocities in the turbulent flow field of a round jet issuing beneath and parallel to a free surface using a three-component laser Doppler velocimeter. They studied the effects of the free surface on the development of a jet below the surface ($h/d = 2$) at a Reynolds number of 12700 and a Froude number of 5.66. The results show that near the jet centreline the velocity fluctuations normal to the surface are reduced while those parallel to the surface are enhanced. They also found that in the presence of a clean free surface a shallow current is formed with a lateral extent greater than the jet flow. The surface current is suppressed by an insoluble surfactant added to the free surface.

Davis & Winarto (1980) studied the interaction of a jet with a solid surface for

different distances between the jet and the solid surface. This geometry is the same as the one studied in the present investigation except for the fact that the free surface is replaced by a solid surface. Davis & Winarto (1980) measured a somewhat higher growth rate in the direction perpendicular to the solid wall and a somewhat lower growth rate in the direction parallel to the solid wall than Rajaratnam & Pani (1974). This work as well as other investigations of the solid wall jet for different jet exit geometries by Sforza & Herbst (1970), Newman *et al.* (1972), Chandrasekhara Swamy & Bandyopadhyay (1975) has been reviewed by Launder & Rodi (1981, 1983).

The significance of the comparison between the wall jet and the free-surface jet is not immediately obvious. The main similarity between these flows is the confinement by the surface which constrains the flow at the free surface or at the wall. However, there are important differences. Water waves can be generated and propagate on a free surface which could not occur on a solid wall. Also, in a wall jet the no-slip boundary condition requires the velocity to be zero at the wall. At a free surface, the velocity can be different from zero and the stress must be continuous (Batchelor 1967). A free-surface boundary layer forms to satisfy this viscous boundary condition. However, this boundary layer is expected to be different from the boundary layer on a solid wall.

In contrast to the jet/free-surface interaction problem the flow characteristics of a turbulent free jet, i.e. in the absence of the free surface, has been the subject of many investigations. The mean and turbulent flow properties in the far field of a turbulent jet have been measured by several investigators, and most extensively by Wygnanski & Fielder (1969). In the far field the maximum mean velocity at each cross-section decays like $1/x$, where x is the distance to the jet exit plane, and the width of the velocity profile is proportional to x. This scaling implies that the flux of downstream momentum is constant along the axis of the flow. Kotsovinos (1976, 1978) and Schneider (1985) have investigated the effect of the momentum flux associated with the entrained fluid. They show a continuous reduction of the momentum flux with downstream distance due to this effect.

The turbulent structure of the free jet has also been studied extensively. In the near field the potential core region is surrounded by a turbulent shear flow region. For an initially laminar shear layer, instability waves grow exponentially and result in the formation of vortex-ring-like structures which interact with each other by amalgamation as they grow downstream. At the end of the potential core, vorticity within these structures reaches the centreline and associated with this process there is a characteristic frequency or preferred mode of the jet (Browand & Laufer 1975; Yule 1978). In the far field of the jet the evidence for the existence of large-scale turbulent structures is convincing (Tso, Kovasznay & Hussain 1981; Dimotakis, Maike-Lye & Papantoniou 1983). However there are a number of unanswered questions regarding the topology and dynamics of these structures. An important motivation for the present study is to characterize the mutual interaction between the free surface and these various turbulent structures.

In the present investigation, we consider the interaction of a circular jet with the free surface for various depths of the jet below the surface. The main objectives of this investigation are: (*a*) to determine the surface waves and motions produced by the interaction of the turbulent jet with the free surface; (*b*) to determine the scaling characteristics of the underwater turbulent jet. Preliminary results of this investigation were reported by Bernal & Madnia (1988).

The presentation of the results is organized as follows. In §2 the flow facility and experimental techniques are described. In §3 the results of a flow visualization study, surface curvature measurements and hot-film velocity measurements are presented. In

§4 these results are discussed and finally, in §5, the main conclusions of the investigation are summarized.

2. Flow facility and measurement techniques

2.1. *Flow facility*

A new free-surface water tank facility was designed and constructed for these experiments. A schematic diagram of the facility is shown in figure 2. It consists of a free-surface tank, a reservoir tank, a jet tank and the associated piping and control valves. The free-surface tank, $76 \times 76 \times 168$ cm, was made of glass and was raised 80 cm above the laboratory floor in order to provide optical access through the bottom of the tank. The water used in the facility was stored in a 1800 l reservoir tank. The jet flow was generated by a jet tank located inside the free surface tank as shown in figure 2. Inside the jet tank a layer of foam 5 cm thick was used to eliminate flow non-uniformities associated with the inlet flow. A circular-arc-shaped nozzle with a radius equal to the wall thickness of the jet tank provides a smooth transition from the sidewall to the jet exit. In continuous operation the large area ratio of the contraction helps reduce the turbulent intensity at the jet exit to a level lower than 0.5%. Three jet tanks were used in the experiments with jet exit diameters of 2.54, 1.27 and 0.64 cm respectively.

The velocity profile at the exit plane of the jet tank was measured and found to be uniform except for a thin boundary layer. The momentum thickness of the boundary layer was estimated using Thwaites method. The calculated values of the boundary-layer Reynolds number showed that the boundary layer was laminar up to values of the velocity $U_e = 200$ cm s^{-1} where it approached the instability point. This was confirmed with shadowgraph images of the flow.

The facility was operated in two different modes. An open-loop configuration was used in flow visualization experiments and in the surface curvature measurements. In this case tap water was stored in the reservoir tank and pumped through the facility into the drain. The water level in the free-surface tank was maintained at the desired level by a stand pipe in the level control box shown in figure 2. The closed-loop configuration was used in the velocity measurements to maintain a constant temperature and water quality during the experiment. In this configuration water in the free-surface tank was recirculated through the jet tank using a pump.

An important limitation of the facility is recirculation caused by confinement of the jet flow in the tank. This limits the maximum velocity and the downstream distance where measurements could be obtained in the experiments. At a fixed downstream location the volume flow entrained by the jet equals the average upstream flow associated with recirculation. A cross-sectional average of this upstream recirculation velocity can be obtained from the entrainment measurements reported by Ricou & Spalding (1961). For example, at $U_e = 200$ cm s^{-1}, $d = 0.64$ cm and $x/d = 40$ the recirculation velocity is 0.23 cm s^{-1} which corresponds to approximately 0.7% of the local maximum mean velocity. This estimate indicates that pressure gradients associated with the recirculation flow can be neglected. In order to determine the acceptable level of recirculation the mean velocity profiles for the deep jet, i.e. $h/d = 24$, were compared to free-jet data in the literature. These results are described in §3.3. On the basis of these comparisons it was concluded that to avoid recirculation effects a conservative value for the jet exit velocity was 200 cm s^{-1} and for the maximum downstream distance was $x = 25$ cm. Additional details on the facility can be found in Madnia (1989).

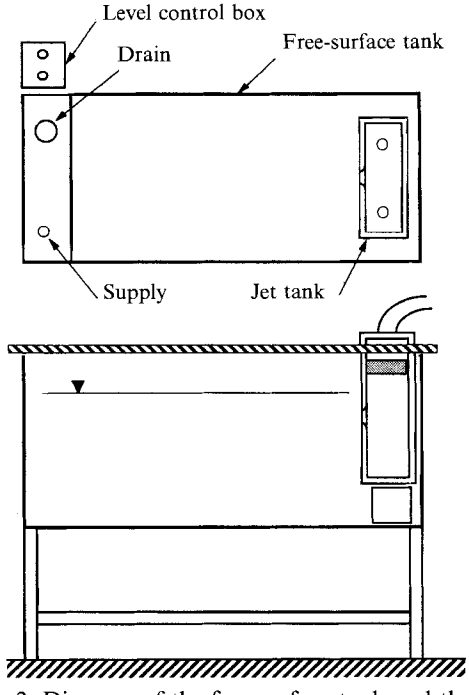

FIGURE 2. Diagram of the free-surface tank and the jet tank.

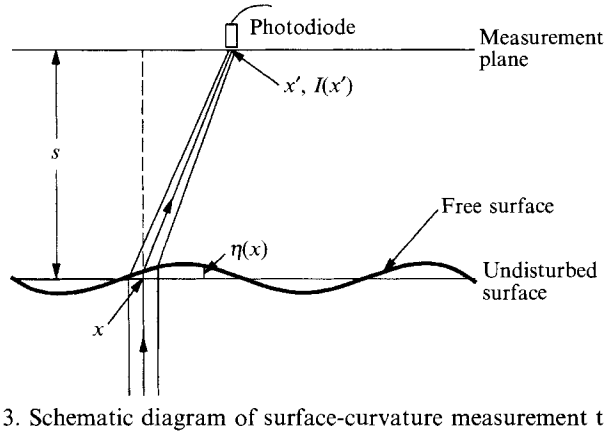

FIGURE 3. Schematic diagram of surface-curvature measurement technique.

2.2. *Flow visualization and surface curvature measurement*

Flow visualization of the free-surface deformation and of the jet fluid was obtained using the shadowgraph technique. A collimated beam of light was formed from the output of a copper vapour laser by means of a focusing lens and a spherical mirror. The collimated beam enters the free-surface tank through the bottom window. Refraction at the water–air interface causes variation in beam intensity in the regions where the free surface is not flat. The resulting shadow image was viewed on a screen located above and close to the free surface. The pictures presented here were obtained by photographing the image on the screen with a 35 mm camera. The jet fluid was simultaneously visualized by using 1 °C cooler water in the jet tank. The corresponding change in the index of refraction results in the light intensity variation typical of shadowgraph images.

Surface curvature measurements were conducted to quantify the various features observed in the flow visualization study. The technique used is based on the same principle as the shadowgraph flow visualization technique. In this case a photodiode was used to measure the temporal fluctuation of the light intensity at a point on the surface, as shown schematically in figure 3. Madnia (1989) discusses the relationship between the surface deformation and the light intensity measured by the photodiode. The light intensity at the photodiode aperture for a two-dimensional deformation of the surface η is given by

$$I(x') = I_0 \left| \frac{dx}{dx'} \right|, \tag{1}$$

where x' is the location of the photodiode and x is the location where the ray captured by the photodiode intersects the surface. Following Madnia (1989) the relationship between x' and x is

$$x' = x + [s - \eta(x)]\,\eta'(x)\,H(x), \tag{2}$$

$$H(x) = \frac{N - [1 - (N^2 - 1)\,\eta'^2]^{\frac{1}{2}}}{[1 - (N^2 - 1)\,\eta'^2]^{\frac{1}{2}} + N\eta'^2}, \tag{3}$$

where s is the distance from the photodiode to the undisturbed water surface, $\eta'(x) = d\eta/dx$ and $N = n_w/n_a$, with n_w the index of refraction of water and n_a the index of refraction of air. For a small amplitude of the surface disturbance dx'/dx is positive for all values of x and, therefore, x' is a single-valued function of x. In the limit of small surface deformations $\eta/s \ll 1$, small surface slope $d\eta/dx \ll 1$ and small surface curvature $s d^2\eta/dx^2 \ll 1$, equations (2) and (3) reduce to

$$I(x') = I_0[1 + s(N-1)\,\rho]. \tag{4}$$

Thus the light intensity measured by the photodiode is proportional to the surface curvature ρ.

As the amplitude of the disturbance increases, the value of dx'/dx can become zero or even negative. When $dx'/dx < 0$, x' is a multivalued function of x which implies that light rays collected by the photodiode propagate through several non-contiguous regions on the water surface. Caustics form at locations where $dx'/dx = 0$. These phenomena limit the use of the technique to small-amplitude surface disturbances.

In the experiments a collimated beam 30 cm in diameter was used to illuminate the surface. A photodiode was positioned above the illuminated region as close as possible to the water surface (0.64 cm) to minimize the formation of caustics. The spatial resolution of the measurements was approximately 1 mm. It was obtained by mounting a small circular aperture 1 mm in diameter in front of the photodiode. The photodiode was operated in reversed bias mode so that the output signal is proportional to the light intensity reaching the aperture. The output signal was DC shifted and amplified using an instrumentation amplifier. For this system the mean value of the photodiode output signal, V_L, is related to the local light intensity of the collimated beam, I_0 and the mean curvature of the water surface. Consistent with the assumption of small surface deformations used in (4), the r.m.s. value of the photodiode output, V_{rms}, normalized by the mean, V_L, is proportional to the r.m.s. amplitude of the surface curvature fluctuations, ρ'. Thus ρ' is given by

$$\rho' = \frac{1}{s(N-1)} \frac{V_{rms}}{V_L}. \tag{5}$$

All the surface curvature data were obtained at the same conditions of illumination,

amplifier gain and with the photodiode at the same distance from the surface. The data were digitized at a typical rate of 200 Hz. The sample duration was of the order of minutes depending on the flow conditions and location of the photodiode.

2.3. *Hot-film velocity measurement*

Velocity data were obtained using a hot-film anemometer. A coated cylindrical sensor was used in the measurements. The sensor length was 0.51 mm and the diameter 25 μm. The signal from the constant-temperature anemometer was DC shifted, amplified and recorded with the same data acquisition system used in the surface-curvature measurements. The hot-film probe was mounted on a computer-controlled traverse mechanism (Willmarth 1977). The resolution of the traverse motion along the axial and transverse directions was 25 μm, and in the vertical direction was 7 μm. In the velocity measurements particular emphasis was placed on ensuring a constant temperature and quality of the water in the tanks to minimize drift of the velocity signal. The velocity signal drift was checked at the end of each traverse across the jet by moving the probe to the exit plane of the jet and measuring the known jet exit velocity. The probe was calibrated in the same free-surface tank facility used in the experiments. The calibration curve was incorporated in the data acquisition software and used to obtain linearized records of the velocity before any additional processing of the signal. The accuracy of the velocity measurements is estimated to be 1 % of the jet exit velocity.

The sensor axis was located parallel to the free surface. To minimize interference with the free surface the probe was tilted backward by 4°. At points close to the surface, depending on the local amplitude of the surface motion the hot-film sensor was intermittently in and out of the water. This resulted in sharp voltage spikes on the time trace of the velocity signal. The spikes were easily identified by signal values outside the calibration range of the sensor. All the velocity data measured at points close to the surface were examined and only data obtained at points where the sensor was continuously submerged are reported.

3. Results

3.1. *Flow visualization*

Typical flow visualization shadowgraph pictures of the jet/free-surface interaction are presented in figures 4–9. In all cases the flow is from left to right. Figures 4–6 were obtained at a jet exit depth corresponding to $h/d = 1$. In these cases the interaction of the jet with the free surface occurs in the near field of the jet. Figure 4 shows the interaction at low jet exit velocity as indicated. Near the jet exit the vortex-ring-like structures can be observed. These structures interact with the free surface and produce characteristic surface deformations which travel with the vortices. The light intensity pattern along the jet centreline in figure 4 indicates a depression of the surface on top of the core of the vortices and an elevation of the surface between the vortices. Farther downstream the jet vortical fluid interacts with the surface. In this region the shadowgraph image of the jet fluid is dominated by the small-scale features in the flow. An interesting feature in this photograph is the two dark spots located at $x/d \approx 4$. The dark spots are due to surface swirls produced by vortex lines normal to the free surface (Berry & Hajnal 1983; Sterling *et al.* 1987). They are generated by the opening and reconnection of vortex lines of the initially submerged ring-like structures. This type of interaction has been investigated by Bernal & Kwon (1989) and Kwon (1989) for axisymmetric vortex rings.

The flow pictures in figures 5 and 6 were obtained at jet exit velocities 35 and

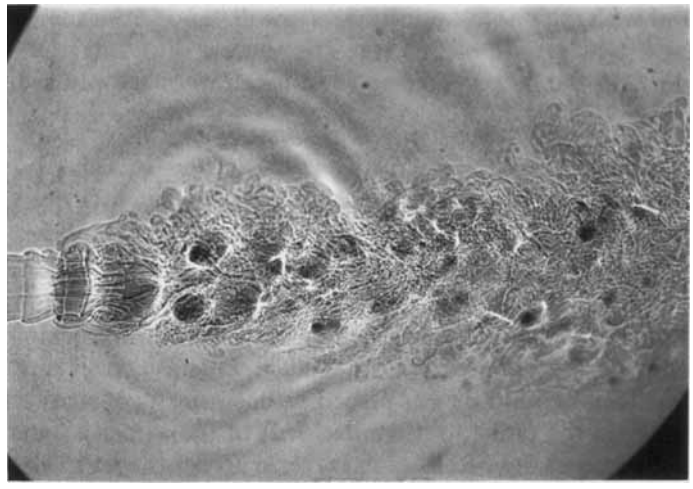

FIGURE 4. Shadowgraph image of the free-surface jet. $U_e = 25$ cm s^{-1}, Reynolds number 6.3×10^3, $U_e/(gh)^{\frac{1}{2}} = 0.5$, $h/d = 1$. Area shown $1 < x/d < 10$.

FIGURE 5. Shadowgraph image of the free-surface jet. $U_e = 35$ cm s^{-1}, Reynolds number 8.9×10^3, $U_e/(gh)^{\frac{1}{2}} = 0.7$, $h/d = 1$. Area shown $1 < x/d < 10$.

50 cm s^{-1} respectively. These pictures show surface wave patterns produced by the interaction of the jet with the free surface. The flow conditions in figure 5 are slightly above the values for which surface waves are first observed. The vortex-ring-like structures moving underneath the surface start deforming the surface at a distance of $x/d \approx 1$, and it is not before a distance of $x/d \approx 4$ that waves are produced. At these flow conditions the waves are produced in the region where vortex lines open in figure 4. The resulting wave fronts propagate in a symmetric pattern at an angle of 39° relative to the downstream direction. Downstream of the wave generation region the turbulence in the jet interacts with the free surface. Dark spots indicating vortex lines terminating at the free surface are observed in this region. At a higher jet exit velocity, in figure 6, the waves are generated over a larger region in the downstream direction. In this case the waves are initially formed at $x/d \approx 4$ and propagate at an angle of 60° relative to the downstream direction. Along the centreline the wavefronts are well defined and are normal to the flow direction. This picture and motion pictures of the

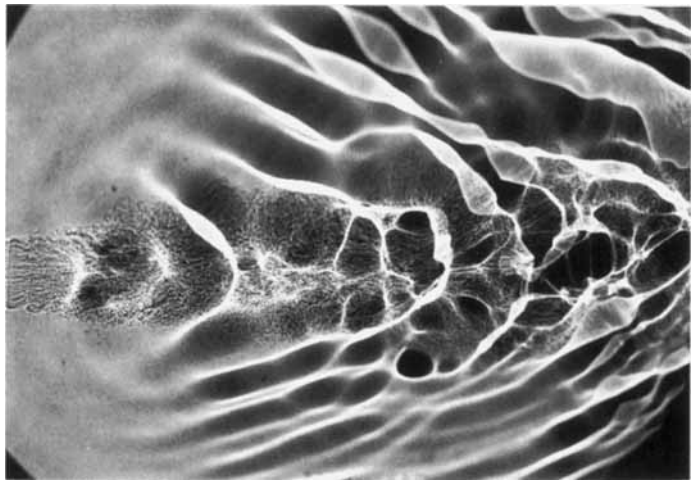

FIGURE 6. Shadowgraph image of the free-surface jet. $U_e = 50$ cm s^{-1}, Reynolds number 1.27×10^4, $U_e/(gh)^{\frac{1}{2}} = 1.0$, $h/d = 1$. Area shown $1 < x/d < 10$.

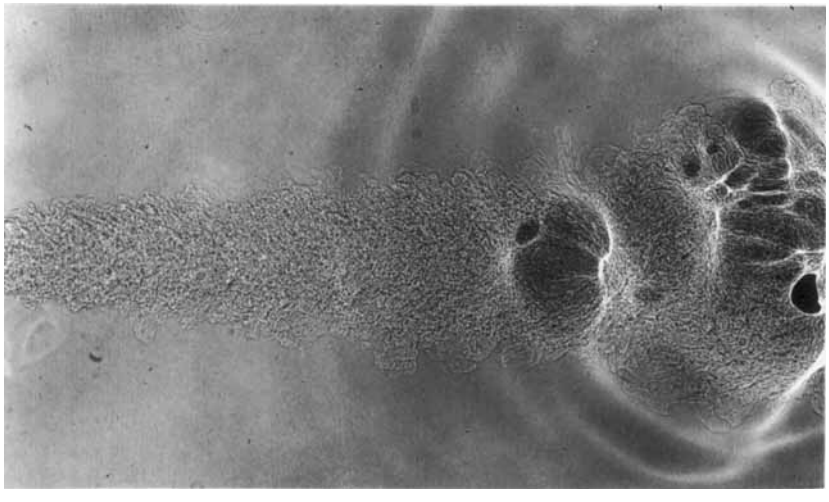

FIGURE 7. Shadowgraph image of the free-surface jet. $U_e = 100$ cm s^{-1}, Reynolds number 1.27×10^4, $U_e/(gh)^{\frac{1}{2}} = 1.5$, $h/d = 3.5$. Area shown $4 < x/d < 24$.

flow obtained at the same flow conditions show an increase of the wavelength of the waves as they propagate along the centreline.

The same features observed in the near-field interaction are also found when the interaction occurs in the far field of the jet. Figure 7 is an instantaneous (1–2 μs) spark shadowgraph picture of the flow field at a Reynolds number of 1.27×10^4 and $h/d = 3.5$. The corresponding jet exit diameter was $d = 1.27$ cm. The shadowgraph image of the flow shows small-scale turbulent structures in the submerged jet fluid. A surface deformation at $x/d \approx 16$ is caused by the interaction of a large-scale vortical structure approaching the surface. The size of this feature is comparable with the local width of the jet. Similar large-scale structures are not captured on the shadowgraph image upstream of the interaction with the free surface. This is because the shadowgraph image of the turbulent region enhances the small-scale structures in the flow. As the turbulent jet reaches the surface refraction effects associated with the surface deformation are more pronounced on the shadowgraph image. This surface

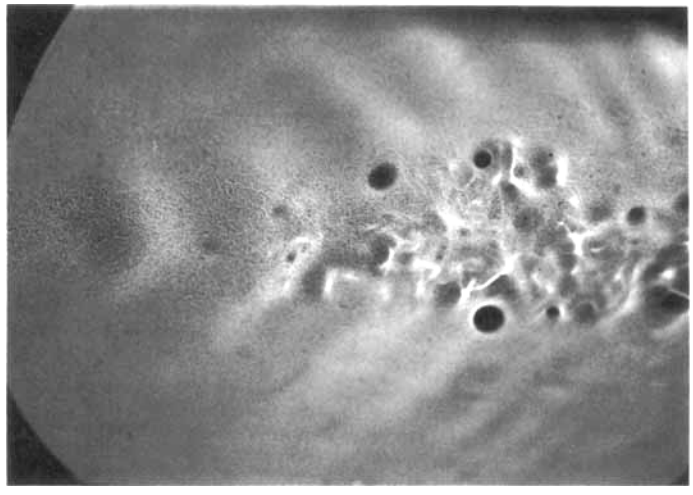

FIGURE 8. Shadowgraph image of the free-surface jet. $U_e = 150$ cm s^{-1}, Reynolds number 9.5×10^3, $U_e/(gh)^{\frac{1}{2}} = 2.6$, $h/d = 5.5$. Area shown $14 < x/d < 52$.

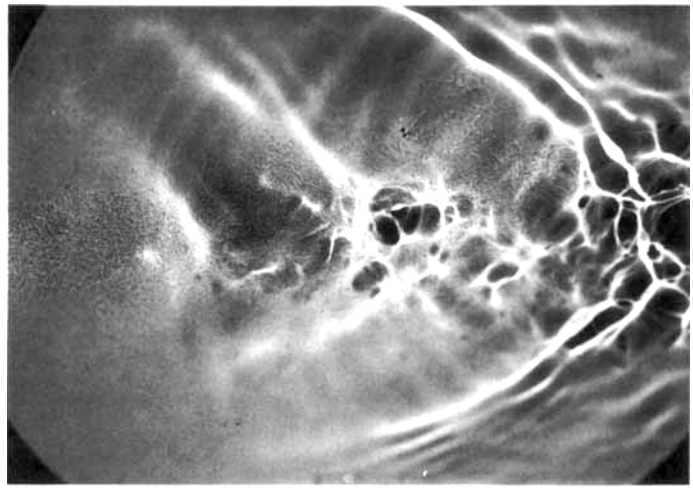

FIGURE 9. Shadowgraph image of the free-surface jet. $U_e = 250$ cm s^{-1}, Reynolds number 1.6×10^4, $U_e/(gh)^{\frac{1}{2}} = 4.3$, $h/d = 5.5$. Area shown $14 < x/d < 52$.

deformation is caused by the large scales in the jet flow. From figure 7 a measure of the visual growth rate of the jet upstream of the interaction can be obtained, which gives a half-angle value of 11°.

Figures 8 and 9 are shadowgraph images of the flow for $h/d = 5.5$ and Reynolds number of 9.5×10^3 and 1.6×10^4 respectively. At the lower jet exit velocity, figure 8 shows surface deformations caused by the large-scale structure in the jet at an axial location of $x/d \approx 25$ on the left side of the photograph. Small-amplitude surface waves are observed propagating at an angle of 42° relative to the downstream direction. Farther downstream the vortical fluid in the large-scale structures breaks the surface resulting in complicated surface patterns ($x/d \approx 33$). Again the dark spots associated with the vortex lines terminating at the free surface are clearly visible in this photograph. At higher jet exit velocity, in figure 9, the surface deformations caused by the large-scale structure in the jet results in larger-amplitude surface waves. The waves propagate at an angle of 54° relative to the downstream direction. In this figure the

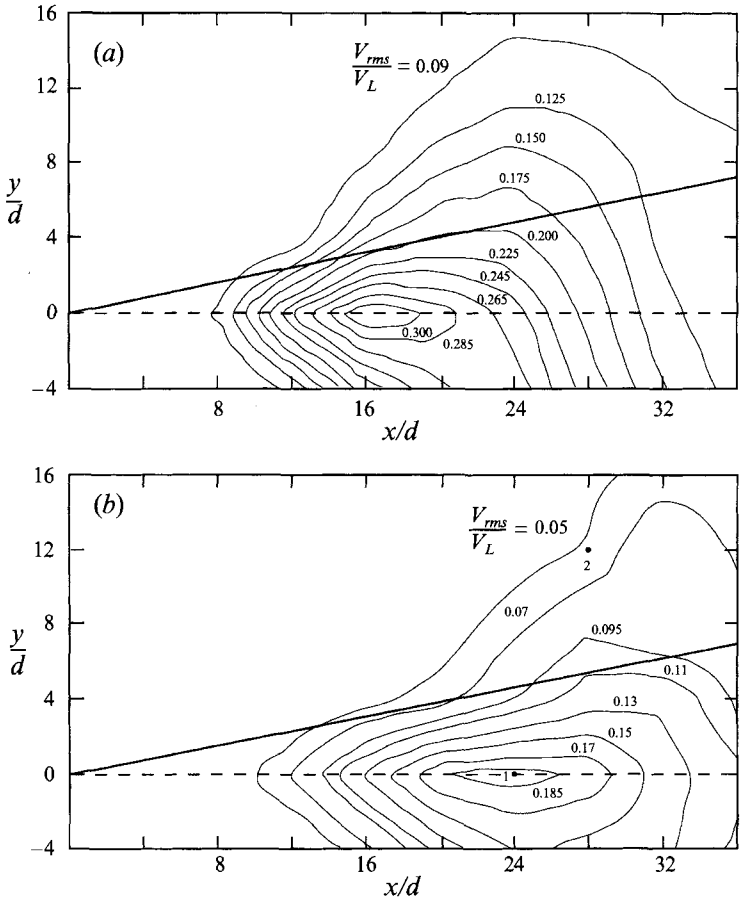

FIGURE 10. Contour plots of V_{rms}/V_L at $U_e = 150$ cm s^{-1}, Reynolds number 9.5×10^3: ——, visual growth of the free jet; – – –, jet centreline. (*a*) $h/d = 2.5$, $U_e/(gh)^{\frac{1}{2}} = 3.8$. (*b*) $h/d = 3.5$, $U_e/(gh)^{\frac{1}{2}} = 3.2$.

wavelength of the surface waves is approximately 7 cm compared to values of the order of 2 cm measured in the near-field interaction of figures 5 and 6. The location where waves are first observed, $x/d \approx 25$, and the location where the vortical fluid breaks the surface, $x/d \approx 33$, are approximately the same as for the low-velocity conditions in figure 8 obtained at the same value of h/d.

3.2. *Surface curvature measurements*

Surface curvature measurements were conducted by locating the photodiode on a matrix of 54 points and recording the temporal fluctuations of light intensity at each point on the surface. An area of 22.9 × 12.7 cm was covered at 2.54 cm intervals. The r.m.s. values of the surface curvature fluctuation (V_{rms}/V_L) were mapped over the region of interaction of the jet with the free surface for several flow conditions. The results for jet velocity of 150 cm s^{-1} and $h/d = 2.5$ and 3.5 are shown in figures 10(*a*) and 10(*b*) respectively. The jet exit diameter was 0.64 cm. These plots are contour plots of constant value of V_{rms}/V_L. Also shown in each plot is a straight solid line which corresponds to the visual growth of the free jet determined from the shadow image in figure 7. A common feature of all contour plots is that along the centreline the r.m.s value reaches a maximum some distance from the nozzle and then decreases farther downstream. This corresponds to the region of maximum surface activity on the flow

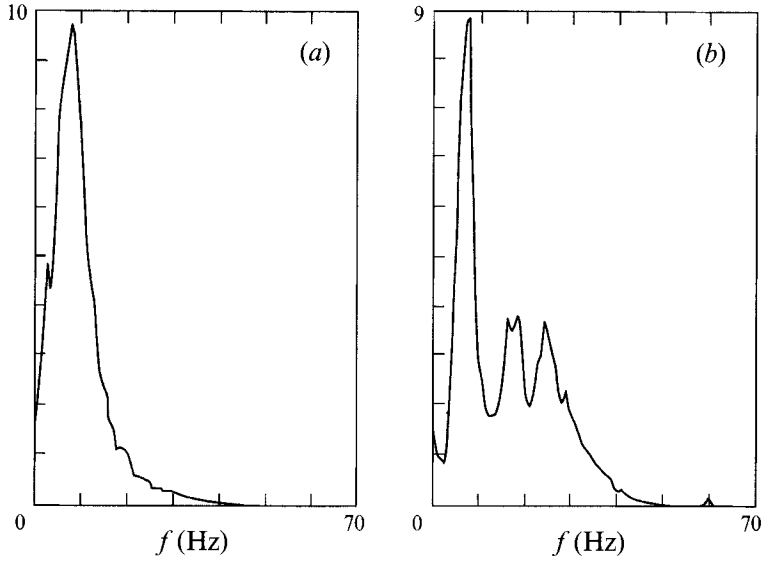

FIGURE 11. Power spectrum of the surface curvature fluctuation measured at two points on the surface at the same flow conditions as points 1 and 2 in figure 10(*b*). (*a*) point 1, (*b*) point 2.

pictures. The lateral extent of the surface-activity region clearly extends beyond the visual growth of the free jet. This is due to the propagation of waves away from the interaction region. The surface area bounded by a contour line for small values of V_{rms}/V_L can be loosely characterized as a sector of a circle. The straight line on the upstream side of the sector corresponds to the direction of propagation of waves at the beginning of the interaction region. This angle changes with flow conditions. Comparison of the contour plots at $h/d = 2.5$ and 3.5 shows that increasing h/d results in a displacement of the interaction region in the downstream direction and a reduction of the maximum value of V_{rms}/V_L. Also, a larger value of h/d results in a smaller propagation angle of the waves.

The surface curvature fluctuations were further characterized with power spectrum measurements along the centreline of the flow and at locations away from the centreline where waves were observed in the pictures. The power spectra were calculated from the time series using Welch's (1967) method. Figure 11(*a*) is a plot of the frequency power spectrum measured on the centreline at $x/d = 24$. This point corresponds to point 1 on figure 10(*b*) in the region of the maximum r.m.s. fluctuation. The vertical axis in the power spectrum plots is normalized with the square of the r.m.s. value so that the area under the curve is unity. There is a distinct peak in the power spectrum at a frequency of 8 Hz. Figure 11(*b*) is the power spectrum measured at $x/d = 28$ and $y/d = 12$ which corresponds to point 2 on figure 10(*b*). The power spectrum shows three distinct peaks at frequencies 8, 16 and 24 Hz. The highest peak occurs at the same frequency as the frequency peak corresponding to point 1 (figure 10*b*) on the centreline. The fact that the frequencies are the same indicates that the measured surface deformations are the result of waves propagating through points 1 and 2 on the surface, consistent with the results of the flow visualization study.

3.3. *Flow velocity measurements*

Experiments were conducted at a jet exit velocity of 200 cm s^{-1} and jet diameter 0.64 cm ($Re = 1.27 \times 10^4$) for depths corresponding to $h/d = 1$, 1.5, 2.5, 3.5 and also 24. The test at $h/d = 24$ was conducted to confirm the free-jet data characteristics in

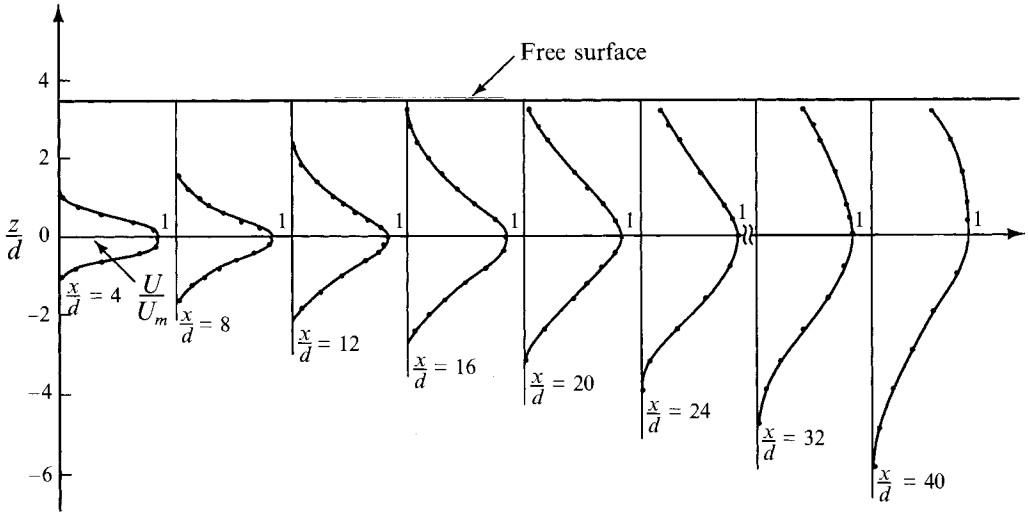

FIGURE 12. Velocity profiles in the direction perpendicular to the free surface. $U_e = 200$ cm s^{-1}, Reynolds number 1.27×10^4, $h/d = 3.5$.

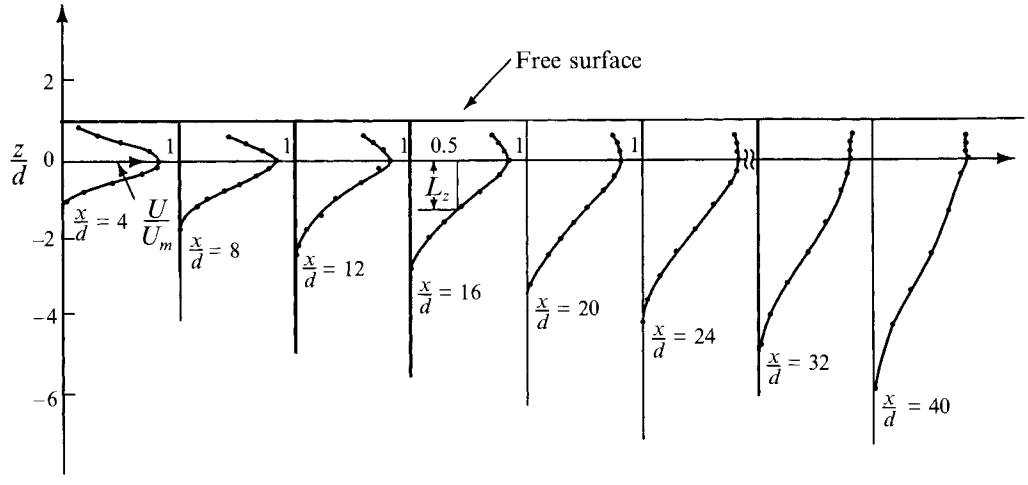

FIGURE 13. Velocity profiles in the direction perpendicular to the free surface. $U_e = 200$ cm s^{-1}, Reynolds number 1.27×10^4, $h/d = 1$.

the facility and to provide basic data for comparisons with the free-surface jet cases. The corresponding values of $U_e/(gh)^{\frac{1}{2}}$ for the free-surface jet cases are 8.0, 6.5, 5.0 and 4.3 respectively.

At each flow condition the mean and r.m.s. value of the velocity fluctuation were measured along directions perpendicular (z-axis) and parallel (y-axis) to the free surface, at several downstream distances. Mean velocity profiles were plotted along the z-direction, figures 12 and 13, and the y-direction, figures 14 and 15, for depth of the jet corresponding to $h/d = 3.5$ and 1 respectively. In all cases the measured mean velocity profiles are normalized by the maximum velocity, U_m, measured at each cross-section. The transverse coordinates measured from the jet centreline are normalized by the jet exit diameter d. Figure 12 shows the velocity profiles measured at $h/d = 3.5$ and several distances from the jet exit plane. The location of the free surface is indicated in the figure. As the flow evolves downstream the jet reaches the free surface resulting in

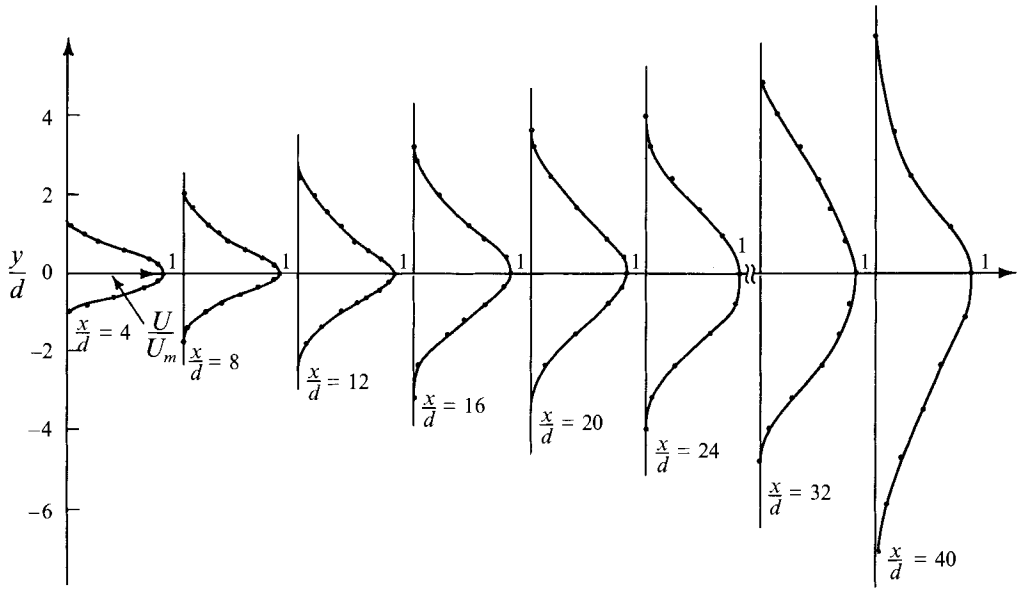

FIGURE 14. Velocity profiles in the direction parallel to the free surface. $U_e = 200$ cm s^{-1}, Reynolds number 1.27×10^4, $h/d = 3.5$.

a mean velocity at the surface different from zero. For $x/d \leqslant 16$ the jet has not reached the surface and the velocity profiles are very similar to the free-jet velocity profiles. Downstream of this station the normalized mean velocity at the point closest to the surface increases. However, at this depth the maximum mean velocity is always found at the centreline of the jet. As the jet is positioned closer to the free surface the interaction occurs closer to the jet exit plane. For $h/d = 1$, figure 13, the interaction begins upstream of $x/d = 4$. The maximum mean velocity for profiles downstream of $x/d = 24$ is not on the centreline and moves towards the free surface. As indicated above, the closest distance to the free surface at which mean data were obtained was 1.9 mm which corresponds to $0.3d$.

The mean velocity profiles in the direction parallel to the free surface are shown in figures 14 and 15 for $h/d = 3.5$ and 1 respectively. These profiles were measured on a plane containing the centreline of the jet. As noted in the discussion of figure 13 the mean velocity on the centreline is not the maximum value measured on the cross-section for $h/d = 1$, $x/d = 32$ and 40. However, at this condition the centreline velocity is very close to the maximum value on the cross-section ($U/U_m \geqslant 0.98$) so that in the plot this value on the centreline cannot be differentiated from unity. At a fixed downstream distance the measured mean velocity profiles for various depths are very similar to each other and also to the profiles measured in the free jet. A more detailed comparison is conducted below in terms of the half-velocity width measured on these profiles.

The downstream evolution of the mean centreline velocity is shown in figure 16 for $h/d = 1$, 1.5, 2.5 and 3.5. The straight line in this plot corresponds to a least squares fit to the free-jet data for $x/d \geqslant 12$ which gives

$$U_e/U_m = 0.162(x/d - 1.9). \tag{6}$$

The slope of this line is in good agreement with results reported in the literature (e.g. Wygnanski & Fiedler 1969; Rajaratnam 1976; Davis & Winarto 1980; Rajaratnam & Humphries 1984). For $x/d \leqslant 16$ the mean centreline velocity in the free-surface jet

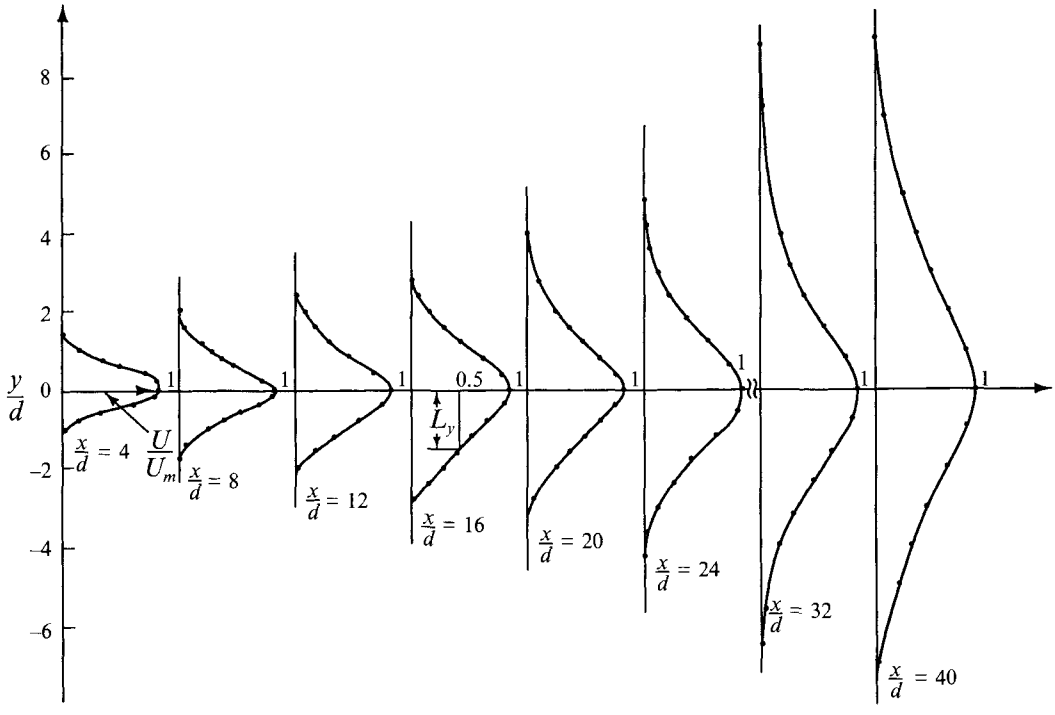

FIGURE 15. Velocity profiles in the direction parallel to the free surface. $U_e = 200$ cm s^{-1}, Reynolds number 1.27×10^4, $h/d = 1$.

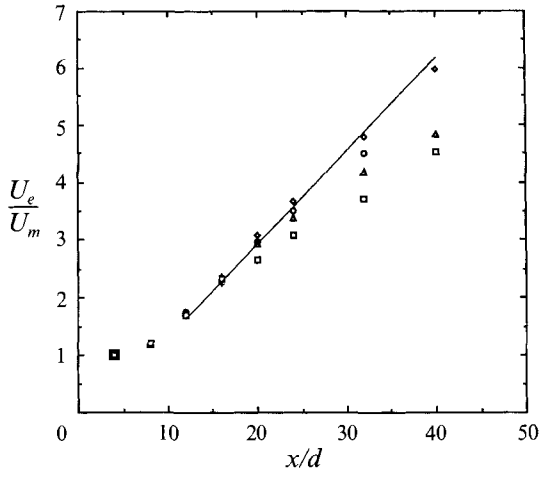

FIGURE 16. Downstream evolution of the maximum mean velocity of the free-surface jet. $U_e = 200$ cm s^{-1}, Reynolds number 1.27×10^4. □, $h/d = 1$; △, $h/d = 1.5$; ○, $h/d = 2.5$; ◇, $h/d = 3.5$; ——, least-squares straight line fit to the free-jet data.

follows the same evolution as the free jet for all values of h/d. Farther downstream the values of U_e/U_m for the free-surface jet are generally lower than the corresponding value for the free jet (solid line). This result implies that the mean centreline velocity decay is slower in the free-surface jet than the free jet. The effect is more pronounced for the smaller values of h/d. For $h/d = 3.5$ the departure from the free-jet data can only be observed for $x/d \geqslant 32$.

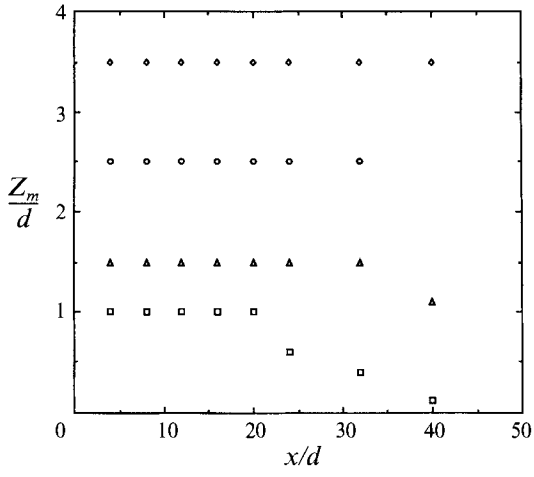

FIGURE 17. Location of the maximum mean velocity as a function of x/d. $U_e = 200$ cm s^{-1}, Reynolds number 1.27×10^4. □, $h/d = 1$; △, $h/d = 1.5$; ○, $h/d = 2.5$; ◇, $h/d = 3.5$.

The mean velocity profiles show a displacement of the location of the maximum mean velocity towards the free surface (see figures 12 and 13). This effect is quantified in figure 17 where Z_m/d is plotted as a function of x/d for the various cases investigated. Z_m is defined as the distance from the location of the maximum mean velocity to the free surface. For $h/d = 2.5$ and 3.5 the location of the maximum mean velocity remains on the centreline, and for $h/d = 1$ and 1.5 the maximum mean velocity moves towards the free surface at $x/d \approx 20$ and 32 respectively. For the case $h/d = 1$ and $x/d = 40$ the location of the maximum mean velocity occurs at the surface within the resolution of these measurements.

The growth rate of the free-surface jet was characterized by the half-velocity width of the mean velocity profiles in the directions perpendicular and parallel to the free surface. The characteristic scales L_y and L_z are defined as the distance from the jet centreline to the location in the profile where the velocity is half the centreline velocity. The definition of L_y and L_z is shown in figures 15 and 13 respectively. The measured half-velocity widths normalized by the jet exit diameter are plotted as a function of x/d in figure 18 for several depths of the jet below the surface. The results for the free jet show the expected linear growth in the far field with the downstream distance, and the same result is obtained in the y- and z-directions. A least-squares fit to the data for $x/d \geqslant 12$ (solid line in figure 18) gives

$$L_z/d = L_y/d = 0.078(x/d + 0.97). \tag{7}$$

This result for the free jet is in good agreement with values reported in the literature (e.g. Wygnanski & Fiedler 1969; Rajaratnam 1976; Davis & Winarto 1980; Rajaratnam & Humphries 1984). The free-surface jet results show values of the half-velocity width lower by as much as 20% compared to the free jet results. In these non-dimensional coordinates the mean velocity results show that the interaction with the surface occurs at different locations depending on h/d. More appropriate non-dimensional parameters are introduced in §4.1 which clarify the evolution of the half-velocity width in the free-surface jet problem.

The good agreement found between the free-jet data in the present facility and data measured in other facilities shows that recirculation effects do not influence the centreline velocity decay or the growth rate of the jet. On the basis of these results it

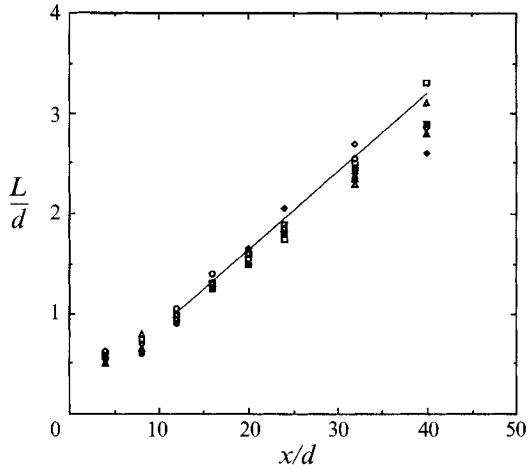

FIGURE 18. Downstream evolution of the half-velocity width for the mean velocity profiles. U_e = 200 cm s^{-1}, Reynolds number 1.27×10^4. □, $h/d = 1$; △, $h/d = 1.5$; ○, $h/d = 2.5$; ◇, $h/d = 3.5$. Solid symbols, L_y/d. Open symbols, L_z/d; ——, least-squares straight line fit to the free-jet data.

was concluded that recirculation effects could be ignored in the present measurements for $U_e \leqslant 200$ cm s^{-1} and for $x \leqslant 25$ cm.

It is interesting to compare these results with the measurements in a wall jet by Davis & Winarto (1980) and Madnia (1989). The growth rate of the wall jet in the direction parallel to the surface is larger than for the free-surface jet by a factor of 3.5. The growth rate in the direction normal to the wall is reduced by a factor of 0.5.

4. Discussion

The interaction of a turbulent jet with the free surface produces a complex pattern of surface waves and motions. This surface pattern is driven by the subsurface turbulent flow. The mean flow characteristics and scaling of this underwater flow are discussed in §4.1. This is followed by the discussion of the free-surface phenomena in §4.2.

4.1. *Mean flow scaling of the free-surface jet*

The jet flow structure was altered as the result of its interaction with the free surface. The evolution of the mean velocity profiles discussed in §3.3 shows a reduction of the decay rate of the maximum velocity as the jet depth is reduced. Also the location of the maximum velocity moves toward the free surface with downstream distance (figure 17). These effects can be attributed to the confinement of the jet flow by the free surface. A simple model of this effect in the limit of high Reynolds number and small Froude number is to treat the free surface as a plane of symmetry (Novikov 1988). Such a model ignores viscous effects at the free surface as well as energy and momentum exchange between the turbulence and the wave field.

The similarity scaling in the far field of the turbulent axisymmetric jet has been discussed by several authors (e.g. Rajaratnam 1976; Tennekes & Lumley 1972; Townsend 1956). If the jet momentum flux is constant, the linear growth of lengthscales with downstream distance implies that sufficiently far downstream compared to the jet exit diameter the mean centreline velocity, U_m, can be written as

$$\left(\frac{J_0}{\rho_0}\right)^{\frac{1}{2}} \frac{1}{U_m} = c_1(x - x_0), \tag{8}$$

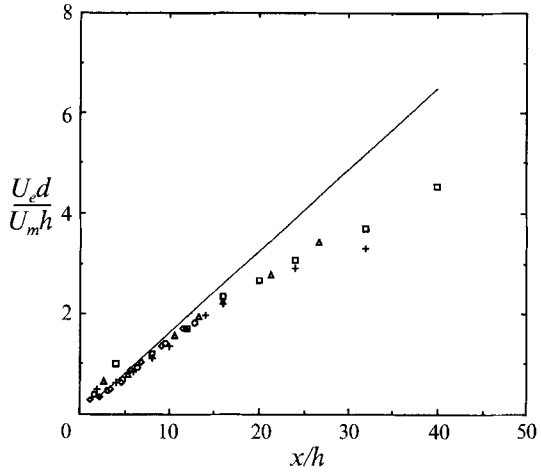

FIGURE 19. Decay of maximum mean velocity for the free-surface jet in similarity variables. U_e = 200 cm s^{-1}, Reynolds number 1.27×10^4. □, $h/d = 1$; △, $h/d = 1.5$; ○, $h/d = 2.5$; ◇, $h/d = 3.5$; ——, free-jet data. +, $h/d = 2.0$ from Anthony & Willmarth (1992).

where ρ_0 is the fluid density and c_1, x_0 are constants determined experimentally. In this investigation the value of $c_1 = 0.162$ was found for the free jet, which is the slope of the solid line on figure 16.

If the free surface is modelled as a plane of symmetry, then the similarity scaling in the far field is that of a jet with twice the momentum of the submerged jet J_0. It follows that for the free-surface jet at sufficiently large distance compared to the jet depth h, the maximum velocity U_m is given by

$$\left(\frac{2J_0}{\rho_0}\right)^{\frac{1}{2}} \frac{1}{U_m} = c_1(x - x_0), \tag{9}$$

where the factor 2 is needed to account for the momentum of the image jet above the surface. The constant c_1 should be the same as for the free jet while the value of x_0 depends on the geometry of the jet and consequently cannot be expected to be the same as for the free jet.

Equation (9) can be written as

$$\frac{U_e d}{U_m h} = \frac{c_1}{\sqrt{2}}\left(\frac{x}{h} - \frac{x_0}{h}\right). \tag{10}$$

This equation is based on the assumption that J_0 is independent of x. As discussed by Kotsovinos (1976, 1978) and Schneider (1985) this assumption fails to account for the momentum flux of the entrained fluid. For a free-surface jet the momentum carried by waves generated at the interaction would result in a lower value of the momentum flux. The presence of surface-active agents (Bernal *et al.* 1989) and surface current effects (Anthony & Willmarth 1992) may also contribute to a reduced momentum flux. To the extent that these effects are small, the similarity argument suggests that: (i) the proper velocity scale for the free-surface axisymmetric jet in the far field is $U_e d/h$; (ii) the proper lengthscale is h, the depth of the jet; and (iii) the maximum mean velocity in the far field is found at the free surface.

Figure 19 is a plot of $U_e d/U_m h$ as a function of x/h for all the cases considered here ($h/d = 1$, 1.5, 2.5 and 3.5) and similar data by Anthony & Willmarth (1992) for

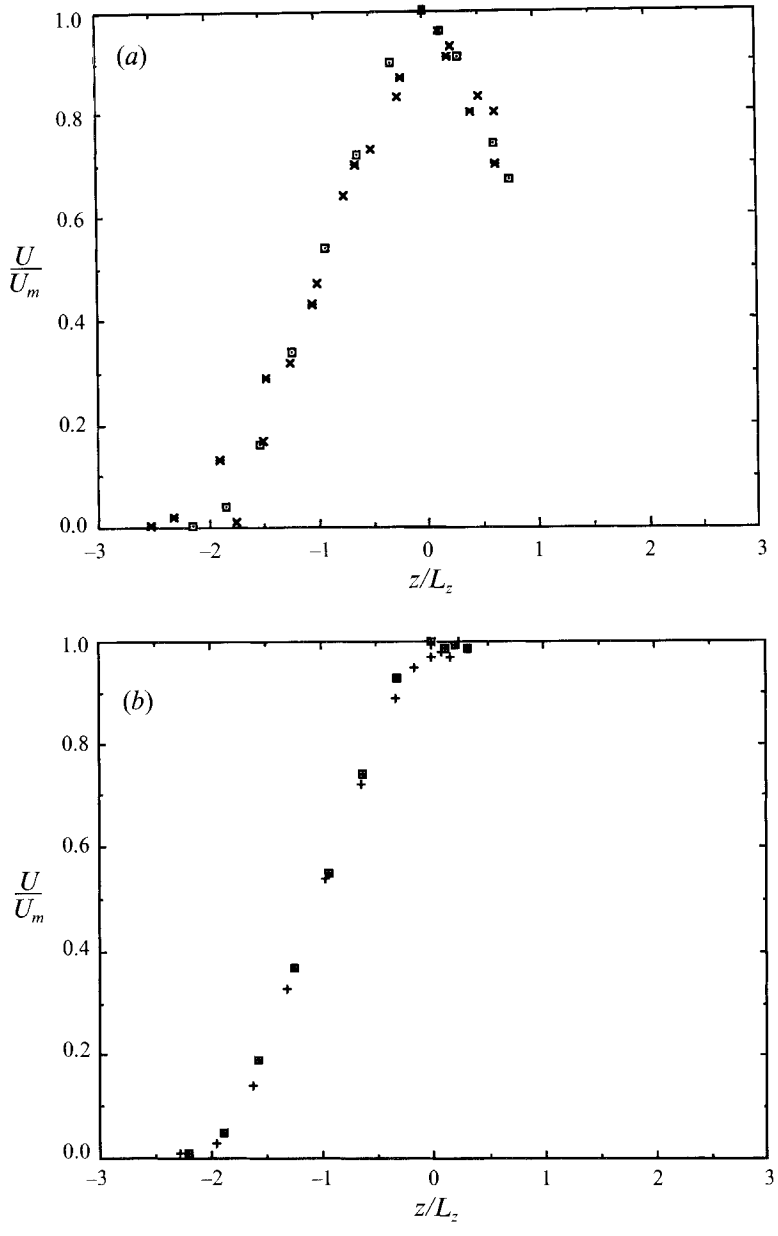

FIGURE 20. Mean velocity similarity profiles normal to the free surface for the free-surface jet. U_e = 200 cm s^{-1}, Reynolds number 1.27×10^4. (*a*) ⊡, $x/h = 10.67$; ⋇, $x/h = 12$; ×, $x/h = 13.33$. (*b*) ⊞, $x/h = 24$; +, $x/h = 32$.

$h/d = 2$ obtained using a laser Doppler velocimeter. It is apparent that the proposed similarity scaling results in good collapse of the data. A least-squares fit to the data for $x/h \geqslant 15$ gives a slope of 0.099. This value is somewhat lower (14%) than the value calculated from $c_1/\sqrt{2} = 0.115$. This lower value of the slope is not consistent with a reduction of momentum flux as would be required by the mechanisms discussed above.

To further examine this difference the mean-velocity similarity profiles in the direction normal to the free surface for various values of x/h are presented in figure 20. Figure 20(*a*) shows a significant reduction of the mean velocity close to the free

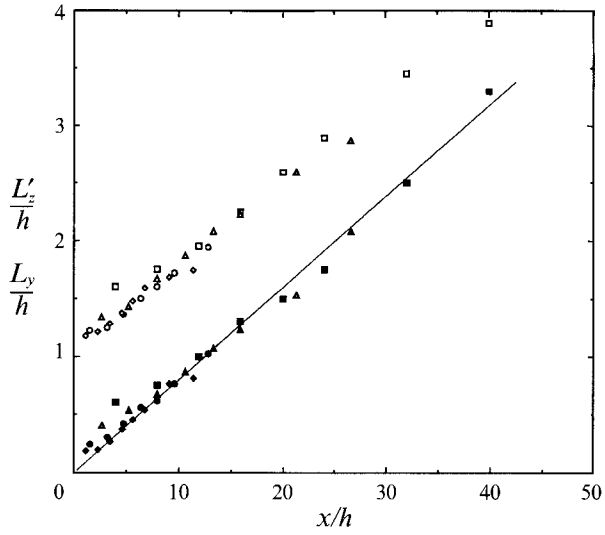

FIGURE 21. Downstream evolution of the half-velocity width of the mean velocity profiles normalized by the jet depth h. $U_e = 200$ cm s^{-1}, Reynolds number 1.27×10^4. □, $h/d = 1$; △, $h/d = 1.5$; ○, $h/d = 2.5$; ◇, $h/d = 3.5$. Solid symbols, L_y/h; open symbols, L_z'/h; ——, least-squares straight line fit to the free-jet data.

surface at $x/h \approx 12$. Clearly this velocity profile is not consistent with the assumptions used to derive (10). Note that $x/h \approx 12$ is where the maximum mean velocity begins to deviate from the free-jet data shown in figure 19. Farther downstream at $x/h = 24$ and 32 the mean velocity similarity profiles are given in figure 20(*b*). These profiles show that the scaling given by (10) can only be valid downstream of $x/h = 32$. If in figure 19 the last two points are used to determine the slope of $U_e d/U_m h$ *vs.* x/h the result is 0.114, which is in good agreement with the value $c_1/\sqrt{2} = 0.115$ derived from the free-jet data.

The results of several investigations have demonstrated the importance of surface contamination effects on the dynamics of vortical flows near a free surface (Bernal *et al.* 1989; Hirsa 1990; Anthony, Hirsa & Willmarth 1991; Kachman 1991). Also velocity measurements of a jet below the free surface by Anthony & Willmarth (1992) show the presence of a thin surface current. The fact that the decay rate of the maximum mean velocity approaches $c_1/\sqrt{2}$ and the good agreement of the present measurements with the results of Anthony & Willmarth indicates that the momentum loss due to these effects is small.

The growth rates of the mean velocity profiles were characterized by the half-velocity widths L_y and L_z in the directions parallel and perpendicular to the free surface. These half-velocity widths were determined with reference to the jet centreline. The arguments presented above suggest that while this definition is adequate for the direction parallel to the free surface, a more appropriate lengthscale in the direction perpendicular to the surface is the half-velocity width measured from the free surface L_z'. The values of L_y/h and L_z'/h are plotted in figure 21 as a function of x/h. The values of L_z'/h (open symbols) are along a line parallel to the L_y/h data but displaced by 1. Both L_y and L_z' grow linearly with x for $x/h < 24$. The growth rates $\mathrm{d}L_y/\mathrm{d}x$ and $\mathrm{d}L_z'/\mathrm{d}x$ are very close to the value for the free jet in this region. However, for $x/h \geqslant 24$ the values of L_y and L_z' start to converge toward each other consistent with the arguments presented above. Similar trends are observed in the data of Anthony & Willmarth (1992). It should be

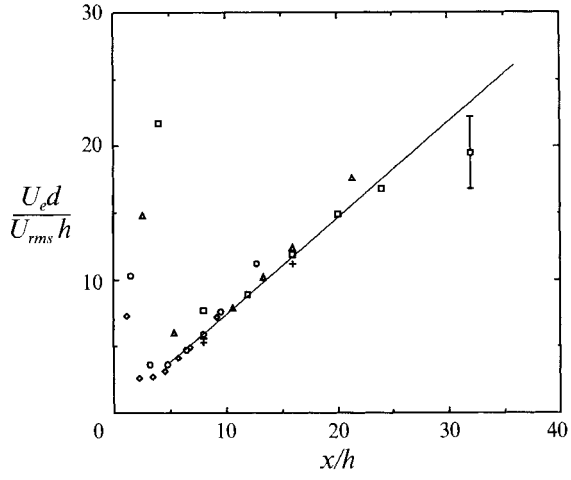

FIGURE 22. Downstream evolution of normalized r.m.s. value of the velocity fluctuation along the centreline of the free-surface jet. $U_e = 200$ cm s^{-1}, Reynolds number 1.27×10^4. □, $h/d = 1$; △, $h/d = 1.5$; ○, $h/d = 2.5$; ◇, $h/d = 3.5$; ——, free-jet data. +, $h/d = 2.0$ from Anthony & Willmarth (1992).

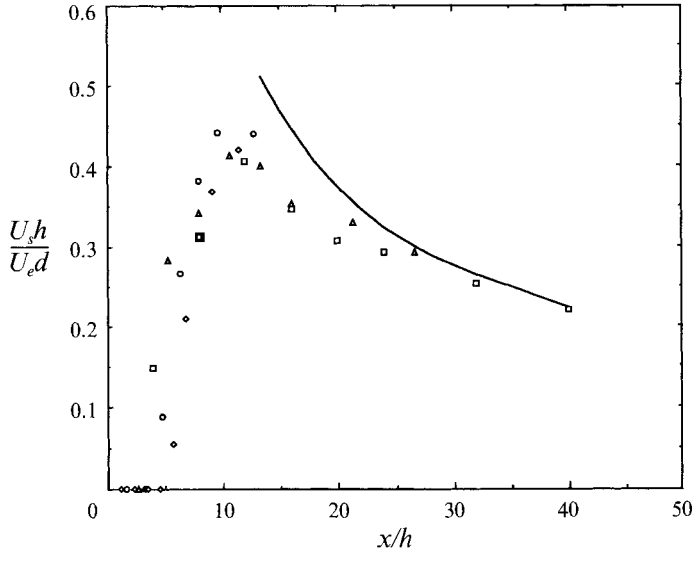

FIGURE 23. Downstream evolution of the normalized mean surface velocity. $U_e = 200$ cm s^{-1}, Reynolds number 1.27×10^4. □, $h/d = 1$; △, $h/d = 1.5$; ○, $h/d = 2.5$; ◇, $h/d = 3.5$; ——, maximum mean velocity.

noted that the values of L_y reported here were measured on the centreline of the jet, below the surface current.

The downstream evolution of the r.m.s. value of the velocity fluctuation normalized by the local mean velocity at the interaction point is shown in figure 22. In this figure $U_e d/U_{rms} h$ is plotted as a function of x/h. This scaling was used because it reduces the uncertainty of the results. Although the uncertainty in the measurement of U_{rms} at $x/h = 32$ is large, there is an indication of a change in the slope of the curve compared to the free-jet data downstream of $x/h = 24$. This is far downstream from $x/h \approx 11$ where the maximum mean velocity starts to deviate from the free-jet line.

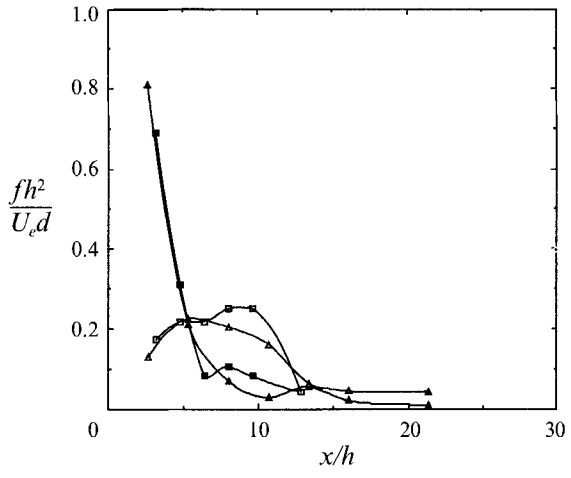

FIGURE 24. Downstream evolution of normalized frequency on the symmetry plane. $U_e = 200$ cm s^{-1}, Reynolds number 1.27×10^4. △, $h/d = 1.5$; ○, $h/d = 2.5$. Solid symbols, frequency of the flow velocity fluctuations. Open symbols, frequency of the surface curvature fluctuations.

Figure 23 is a plot of the mean surface velocity along the jet centreline measured at a distance of approximately 2 mm below the surface. The mean surface velocity is very small for $x/h \leqslant 5$, reaches a maximum at $x/h \approx 11$ and decreases downstream of this point. The solid line in this plot corresponds to the maximum mean velocity data presented in figure 19. Figure 23 shows that the rate of decay of the surface velocity is much slower than its initial rate of increase upstream of $x/h \approx 11$ and approaches the value for the maximum mean velocity at $x/h \approx 30$.

4.2. *Surface waves and surface motions*

The main objective of this investigation was to determine the nature of the free-surface motions caused by the interaction of turbulence in the underwater jet with the free surface. One of the important aspects of this interaction is the generation of the surface waves. These waves are produced by the large-scale vortical motion moving underneath and approaching the surface, initially deforming it and eventually 'breaking' the surface. The series of events leading to the generation of surface waves observed on the motion pictures of the flow are illustrated in figures 4–9. Additional evidence can be found in the results presented in figures 24, 25 and table 1. In figure 24 the frequency of the peak power spectral density of the surface deformation and of the velocity fluctuations measured on the jet axis are compared. Figure 25 is the plot of the normalized r.m.s. amplitude of the surface curvature plotted as a function of x/h for several flow conditions.

Figure 24 shows that the surface waves form at the same frequency as the underwater large-scale motion at $x/h \approx 5$. At this location the mean surface velocity is very small, as shown in figure 23, while the surface-curvature results in figure 25 indicate significant amplitude of the surface deformation. It follows that this initial surface deformation is produced before the underwater vortical flow has reached the surface. This type of interaction has been investigated by Tryggvason (1988).

Farther downstream ($5 < x/h < 12$) the frequency of the surface curvature fluctuations remains approximately constant while the frequency of the velocity fluctuations decreases. This result implies that the surface deformation is dominated by waves generated upstream propagating into this region. The amplitude of the surface

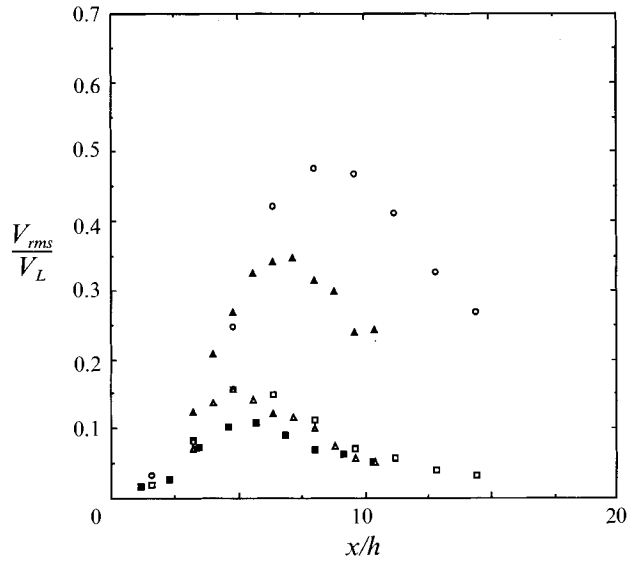

FIGURE 25. Downstream evolution of the r.m.s. value of the surface curvature fluctuation along the jet centreline. □, $U_e = 100$ cm s^{-1}, $d = 0.64$ cm, $h/d = 2.5$; ■, $U_e = 100$ cm s^{-1}, $d = 0.64$ cm, $h/d = 3.5$; ○, $U_e = 200$ cm s^{-1}, $d = 0.64$ cm, $h/d = 2.5$; △, $U_e = 100$ cm s^{-1}, $d = 1.27$ cm, $h/d = 2.5$; ▲, $U_e = 150$ cm s^{-1}, $d = 1.27$ cm, $h/d = 2.5$.

U_e (cm s^{-1})	h/d	d (cm)	$\frac{x_m}{h}$	$\frac{f_s h^2}{U_e d}$	$\frac{f_w h^2}{U_e d}$	$\frac{x_w}{d}$	$\frac{y_w}{d}$	$\frac{U_e d}{U_w h}$
50	1.0	0.64	4.0	0.38	0.38	12.0	8.0	2.16
50	1.0	1.27	8.0	0.38	0.38	12.0	6.0	2.16
100	1.5	1.27	6.67	0.29	0.29	16.0	8.0	2.87
100	2.5	1.27	5.20	0.40	0.48	16.0	6.0	1.72
100	2.5	0.64	4.80	0.40	0.40	32.0	12.0	1.72
100	3.5	0.64	5.71	0.47	0.50	32.0	12.0	1.23
150	2.5	0.64	6.40	0.27	0.27	32.0	12.0	2.59
150	3.5	0.64	6.86	0.42	0.42	28.0	12.0	1.85
200	2.5	0.64	8.0	0.24	0.20	32.0	12.0	3.45
200	3.5	0.64	6.86	0.31	0.31	24.0	12.0	2.46

TABLE 1. Summary of surface motion and wave data

deformation has a maximum in this region, as shown in figure 25. The normalized frequency $f_s h^2/U_e d$ and location x_m/h at the maximum interaction obtained from the surface-curvature measurements are given in table 1. Also relevant is the observation in figure 23 that the surface velocity reaches a maximum at $x/h \approx 11$. Thus the waves propagating along the centre-plane encounter an increase followed by a reduction of the surface mean velocity. This acceleration and deceleration of the flow implies straining of the surface. In the absence of a mean surface deformation

$$\frac{\partial U_s}{\partial x} + \frac{\partial V_s}{\partial y} = 0. \tag{11}$$

Therefore the surface flow is accelerating, $\partial U_s/\partial x > 0$, in the region $5 < x/h < 12$ (see figure 23). In this region there is stretching of the surface in the axial direction and

contraction in the lateral direction. Farther downstream when the surface flow decelerates, $\partial U_s/\partial x < 0$, there is contraction of the surface in the axial direction and stretching of the surface in the lateral direction.

The effect of the surface currents on the waves has been studied by Evans (1955), Taylor (1955), Hughes & Stewart (1961), Longuet-Higgins & Stewart (1961), Taylor (1962) and Peregrine (1976). Their results are discussed by Phillips (1966). They found that when waves propagate over a surface with non-uniform currents, the waves undergo changes in wavelength, amplitude and direction. The effect of increased surface velocity on the waves can be observed in figure 6. The distance between the wave crests increases along the jet centreline. Also there is an indication of a decrease in the curvature of the crests and wave amplitude along this direction. These data suggest that surface straining hinders the propagation and generation of surface waves on the centreline region of the jet downstream of $x/h \approx 11$.

Farther downstream, for $x/h > 11$, figure 24 indicates that the surface curvature fluctuations occur at the same frequency as the underwater flow field. In this region the surface motion follows the fluctuations of the underwater turbulence. The amplitude of the fluctuations decreases monotonically with downstream distance. A conspicuous feature of the interaction of the vortical structures with the surface are the dark spots associated with the vortex lines terminating at the free surface. Since the fluid at the free surface is initially irrotational, vorticity at the free surface must be the result of the interaction of the vortical flow under the surface with the free surface. Figure 4 is a typical photograph of this interaction, in which underwater vortex lines in the near field of the jet open at the free surface. This type of interaction is important because it not only imparts momentum to the surface but also because of the associated mass transport. These flow processes in the simpler case of a vortex ring have been investigated by Bernal & Kwon (1989) and Kwon (1989).

The waves generated by the underwater flow also propagate away from the centreline. The dominant frequency in the wave region, f_w, and at the point of maximum interaction, f_s, were obtained from the power spectrum of the surface curvature data. The results for various jet exit velocities and depths presented in table 1 show good agreement between these two frequencies. The wavelength of the waves was calculated using the dispersion relation for the deep water waves with surface tension as well as gravity taken into account (Lighthill 1978). The wavelengths obtained were approximately 1–7 cm in the capillary–gravity range. These values are in agreement with the flow visualization results. The Strouhal number corresponding to the cases for which the waves were generated in the near field of the jet (i.e. $h/d = 1$) was calculated to be $St = f_w d/U_e = 0.38$. This value of the Strouhal number falls within the range of $St = 0.24$–0.64 corresponding to the preferred mode for jets (Gutmark & Ho 1983). As the jet depth is increased the Strouhal number defined as $St = f_w h^2/U_e d$ is more appropriate. The values of this Strouhal number are given in table 1; they are in the range 0.20–0.48.

The propagation characteristics of the waves show a number of interesting features. The flow visualization and frequency results discussed earlier show that the waves are generated by the large-scale vortical structures in the flow before they reached the free surface. It follows that the propagation angle of the waves is determined by the ratio of the advection speed of the large-scale vortical structures in the flow to the speed of propagation of surface waves at the frequency of the large-scale motion. Thus for a fixed depth, as the jet exit velocity is increased the advection velocity and frequency of the large-scale structures is increased. As the frequency of the subsurface disturbances increases the phase speed of the waves is reduced. These two effects result in an

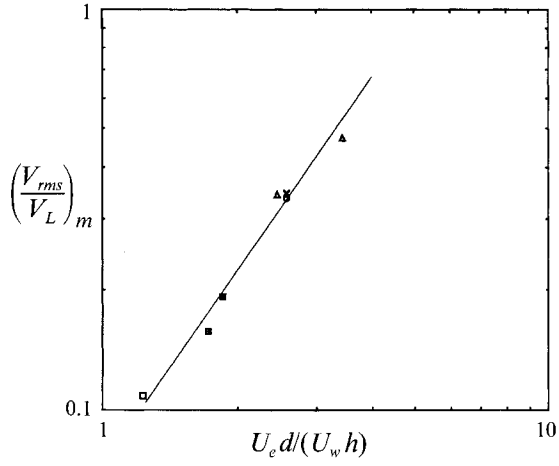

FIGURE 26. Maximum r.m.s. surface curvature fluctuation as a function of $U_e d/(U_w h)$. □, U_e = 100 cm s^{-1}, d = 0.64 cm; ○, U_e = 150 cm s^{-1}, d = 0.64 cm; △, U_e = 200 cm s^{-1}, d = 0.64 cm; ×, U_e = 150 cm s^{-1}, d = 1.27 cm; +, U_e = 100 cm s^{-1}, d = 1.27 cm; ——, least-squares fit to the data.

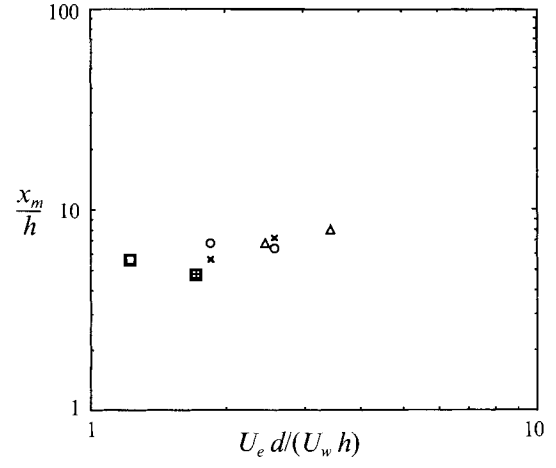

FIGURE 27. Location of the maximum r.m.s. surface curvature fluctuation as a function of $U_e d/U_w h$. For key to the symbols see the caption of figure 26.

increase of the propagation angle relative to the downstream direction. These arguments are consistent with the flow visualization results of §3.1 which show a wave propagation angle of approximately 60° for U_e = 50 cm s^{-1} and $h/d = 1$ compared to 39° for U_e = 35 cm s^{-1} and $h/d = 1$. The results of the surface curvature measurements (figures 10*a* and 10*b*) also show a steepening of the wave propagation angle with strength of the interaction.

The measurements of the surface curvature show an increase followed by a reduction of the amplitude of the surface curvature fluctuations with downstream distance (figure 25). As the 'strength' of the interaction is increased, say by increasing the jet exit velocity keeping the other parameters constant, the maximum value of the surface curvature fluctuation $(V_{rms}/V_L)_m$, increases in magnitude and its location, x_m, moves downstream. These changes are documented in figures 26 and 27 for $(V_{rms}/V_L)_m$ and x_m/h respectively. In both figures the 'strength' of the interaction is characterized by

the parameter $U_e d/U_w h$, where $U_e d/h$ is the characteristic velocity for the free-surface jet and U_w is the minimum phase velocity of capillary–gravity waves. U_w is used because at the conditions of the experiments reported here both capillary and gravity effects are important in the dynamics of the surface waves and motions. The use of the gravity wave scaling $(gh)^{\frac{1}{2}}$ is not appropriate. A least-squares fit to the data in figure 26 shows that the increase in $(V_{rms}/V_L)_m$ is proportional to $(U_e d/U_w h)^{1.6}$. The downstream location of the maximum interaction point approaches a value of $x_m/h \approx 10$ for $U_e d/U_w h \approx 4$. Although these data were obtained at comparatively low Froude numbers, it appears that x_m/h will not increase beyond $x/h = 11$ where the maximum surface velocity is found.

5. Conclusions

The objective of this investigation was to study the free-surface motions caused by the interaction of a turbulent jet with the free surface. It was found that surface waves are generated by the vortical structures in the jet. Surface deformations are first observed at $x/h = 1$–2. Surface waves form in a symmetric pattern at $x/h = 4$–5. For the conditions investigated here the wavelength of the waves was in the range 1–7 cm in the capillary–gravity range. The waves propagate at an angle with respect to the flow direction which increases as the Froude number is increased. Propagation of the waves is inhibited by surface currents produced by the jet flow downstream of $x/h = 10$. In this region the turbulence in the jet produces surface deformations. An interesting feature of these interactions is the formation of surface swirls due to vorticity normal to the free surface. Vortex line reconnection processes are believed to be the mechanism of generation of these features.

The scaling parameters for the free-surface jet were determined. They are the jet depth, h, and the characteristic velocity at the interaction $U_e d/h$. The decay rate of maximum mean velocity in the far field is reduced by a factor of $\sqrt{2}$ compared to the free jet. The mean growth rate of the free-surface jet in the initial region ($x/h \leqslant 24$) and below the surface current is approximately the same as for the free jet. These results indicate that momentum loss in the interaction region due to surface contamination, wave generation and the momentum flux associated with the surface current are small. Comparison with wall-jet data shows significant differences attributed to momentum loss due to friction at the wall as discussed by Madnia (1989). The scaling arguments and data presented above show that the relevant parameter characterizing the strength of the interaction is $U_e d/U_w h$.

This work was supported by the Office of Naval Research, Contract No. N000184-86-k-0684 under the University Research Initiative – Program for Ship Hydrodynamics, and Contract No. N00014-92-J-1750.

REFERENCES

ANTHONY, D. G., HIRSA, A., & WILLMARTH, W. W. 1991 On the interaction of a submerged turbulent jet with a clean or contaminated free surface. *Phys. Fluids* A **3**, 245–247.

ANTHONY, D. G. & WILLMARTH, W. W. 1992 Turbulence measurements in a round jet beneath a free surface. *J. Fluid Mech.* **243**, 699–720.

BATCHELOR, G. K. 1967 *An Introduction to Fluid Dynamics*. Cambridge University Press.

BERNAL, L. P., HIRSA, A., KWON, J.T. & WILLMARTH, W. W. 1989 On the interaction of vortex rings and pairs with a free surface for varying amounts of surface active agent. *Phys. Fluids* A **1**, 2001–2004.

BERNAL, L. P. & KWON, J. T. 1989 Vortex ring dynamics at a free surface. *Phys. Fluids* A **1**, 449–451.

BERNAL, L. P. & MADNIA, C. K. 1988 Interaction of a turbulent round jet with the free surface. In *Proc. 17th Symp. on Naval Hydrodynamics,* pp. 79–87. Washington: National Academy Press.

BERRY, M. V. & HAJNAL, J. V. 1983 The shadows of floating objects and dissipating vortices. *Optica Acta* **30**, 23–40.

BROWAND, F. K. & LAUFER, J. 1975 The role of large scale structures in the initial development of circular jets. In *Proc. 4th Symp. on Turbulence in Liquids, University of Missouri-Rolla* (ed. J. L. Zakin & G. K. Patterson).

CHANDRASEKHARA SWAMY, N. V. & BANDYOPADHYAY, P. 1975 Mean and turbulence characteristics of three-dimensional wall jets. *J. Fluid Mech.* **71**, 541–562.

DAVIS, M. R. & WINARTO, H. 1980 Jet diffusion from a circular nozzle above a solid plane. *J. Fluid Mech.* **101**, 201–221.

DIMOTAKIS, P. E., MAIKE-LYE, R. C. & PAPANTONIOU, D. A. 1983 Structure and dynamics of round turbulent jets. *Phys. Fluids* **26**, 3185–3192.

EVANS, J. T. 1955 Pneumatic and similar breakwaters. *Proc. R. Soc. Lond.* A **231**, 457–466.

GUTMARK, E. & HO, C.-M. 1983 Preferred modes and spreading rates of jets. *Phys. Fluids* **26**, 2932–2938.

HIRSA, A. 1990 An experimental investigation of vortex pair interaction with a clean or contaminated free surface. PhD thesis, University of Michigan.

HUGHES, B. A. & STEWART, R. W. 1961 Interaction between gravity waves and shear flow. *J. Fluid Mech.* **10**, 385–400.

KACHMAN, N. J. 1991 The interaction of a vortex ring with a contaminated free surface. PhD thesis, University of Michigan.

KOTSOVINOS, N. E. 1976 A note on the spreading rate and virtual origin of a plane turbulent jet. *J. Fluid Mech.* **77**, 305–311.

KOTSOVINOS, N. E. 1978 A note on the conservation of the axial momentum of a turbulent jet. *J. Fluid Mech.* **87**, 55–63.

KWON, J. T. 1989 Experimental study of vortex ring interaction with a free surface. PhD thesis, University of Michigan.

LAUNDER, B. E. & RODI, W. 1981 The turbulent wall jet. *Prog. Aerospace Sci.* **19**, 81–128.

LAUNDER, B. E. & RODI, W. 1983 The turbulent wall jet – measurements and modeling. *Ann. Rev. Fluid Mech.* **15**, 429–459.

LIGHTHILL, J. 1978 *Waves in Fluids.* Cambridge University Press.

LONGUET-HIGGINS, M. S. & STEWART, R. W. 1961 The changes in amplitude of short gravity waves on steady non-uniform currents. *J. Fluid Mech.* **10**, 529–549.

MADNIA, C. K. 1989 Interaction of a turbulent round jet with the free surface. PhD thesis, University of Michigan.

MUNK, W. H., SCULLY-POWER, P. & ZACHARIASEN, F. 1987 The Bakerian Lecture 1986: Ships from space. *Proc. R. Soc. Lond.* A **412**, 231–254.

NEWMAN, B. G., PATEL, R. P., SAVAGE, S. B. & TJIO, H. K. 1972 Three dimensional wall jet originating from a circular orifice. *Aero. Q.* **23**, 188–200.

NOVIKOV, E. A. 1988 Generation of water waves by three-dimensional vortex structures. *Phys. Lett.* A **130**, 138–140.

PEREGRINE, D. H. 1976 Interaction of water waves and currents. *Adv. Appl. Mech.* **16**, 9–117.

PHILLIPS, O. M. 1966 *The Dynamics of the Upper Ocean.* Cambridge University Press.

RAJARATNAM, N. 1976 *Turbulent Jets.* Elsevier.

RAJARATNAM, N. & HUMPHRIES, J. A. 1984 Turbulent non-buoyant surface jets. *J. Hydraul. Res.* **22**, 103–115.

RAJARATNAM, N. & PANI, B. S. 1974 Three dimensional turbulent wall jets. *Proc. ASCE, J. Hyd. Div.* **100**, 69–83.

RAMBERG, S. E., SWEAN, T. F. & PLESNIA, M. W. 1989 Turbulence near a free surface in a plane jet. *Naval Research Lab. Mem. Rep.* 6367.

RICOU, F. P. & SPALDING, D. B. 1961 Measurements of entrainment by axisymmetrical turbulent jets. *J. Fluid Mech.* **11**, 21–32.

SCHNEIDER, W. 1985 Decay of momentum flux in submerged jets. *J. Fluid Mech.* **154**, 91–110.

SFORZA, M. P. & HERBST, G. 1970 A study of three-dimensional, incompressible turbulent wall jets. *AIAA J.* **8**, 276–282.

STERLING, M. H., GORMAN, M., WIDMANN, P. J., COFFMAN, S. C., STROZIER, J. & KIEHN, R. M. 1987 Why are these disks dark? The optics of Rankine vortices. *Phys. Fluids* **30**, 3624–3626.

TAYLOR, G. I. 1955 The action of surface current used as a breakwater. *Proc. R. Soc. Lond.* A **231**, 466–478.

TAYLOR, G. I. 1962 Standing waves on a contracting or expanding current. *J. Fluid Mech.* **13**, 182–192.

TENNEKES, H. & LUMLEY, J. L. 1972 *The First Course in Turbulence.* MIT Press.

TOWNSEND, A. A. 1956 *The Structure of Turbulent Shear Flow.* Cambridge University Press.

TRYGGVASON, G. 1988 Deformation of a free surface as a result of vortical flows. *Phys. Fluids* **31**, 955–957.

TSO, J., KOVASZNAY, L. S. G. & HUSSAIN, A. K. M. F. 1981 Search for large scale coherent structures in the nearly self-preserving region of a turbulent axisymmetric jet. *Trans. ASME* I: *J. Fluids Engng* **103**, 503–508.

WELCH, P. D. 1967 The use of fast Fourier transform for the estimation of power spectra: A method based on time averaging over short, modified periodograms. *IEEE Trans. Audio Electroacoust.* **AU-15**, No. 2. 70–73.

WILLMARTH, W. W. 1977 The effect of cross flow and isolated roughness elements on the boundary layer and wall pressure fluctuation on circular cylinders. *University of Michigan Dept. of Aerospace Engng Rep.* 014439-01, 4.

WYGNANSKI, I. & FIEDLER, H. E. 1969 Some measurements in the self-preserving jet. *J. Fluid Mech.* **38**, 577–612.

YULE, A. J. 1978 Large-scale structure in the mixing layer of a round jet. *J. Fluid Mech.* **89**, 413–432.